Journal of Controlled Release 328 (2020) 805–816

Contents lists available at ScienceDirect

Journal of Controlled Release

journal homepage: www.elsevier.com/locate/jconrel

Optical imaging of the whole-body to cellular biodistribution of clinical-stage PEG-b-pHPMA-based core-crosslinked polymeric micelles

Ilaria Biancacci[a,1], Qingxue Sun[a,1], Diana Möckel[a,b,1], Felix Gremse[a,b], Stefanie Rosenhain[a,b], Fabian Kiessling[a], Matthias Bartneck[c], Qizhi Hu[d], Marielle Thewissen[d], Gert Storm[e,f,g], Wim E. Hennink[e], Yang Shi[a], Cristianne J.F. Rijcken[d,*], Twan Lammers[a,e,f,**], Alexandros Marios Sofias[a,**]

[a] Department of Nanomedicine and Theranostics, Institute for Experimental Molecular Imaging, Faculty of Medicine, RWTH Aachen University, Aachen, Germany
[b] Gremse-IT GmbH, Aachen, Germany
[c] Department of Internal Medicine III, University Hospital RWTH Aachen, Aachen, Germany
[d] Cristal Therapeutics, Maastricht, the Netherlands
[e] Department of Pharmaceutics, Utrecht University, Utrecht, the Netherlands
[f] Department of Targeted Therapeutics, University of Twente, Enschede, the Netherlands
[g] Department of Surgery, Yong Loo Lin School of Medicine, National University of Singapore, Singapore

A B S T R A C T

Core-crosslinked polymeric micelles (CCPM) based on PEG-b-pHPMA-lactate are clinically evaluated for the treatment of cancer. We macroscopically and microscopically investigated the biodistribution and target site accumulation of CCPM. To this end, fluorophore-labeled CCPM were intravenously injected in mice bearing 4T1 triple-negative breast cancer (TNBC) tumors, and their localization at the whole-body, tissue and cellular level was analyzed using multimodal and multiscale optical imaging. At the organism level, we performed non-invasive 3D micro-computed tomography-fluorescence tomography (μCT-FLT) and 2D fluorescence reflectance imaging (FRI). At the tissue and cellular level, we performed extensive immunohistochemistry, focusing primarily on cancer, endothelial and phagocytic immune cells. The CCPM achieved highly efficient tumor targeting in the 4T1 TNBC mouse model (18.6 %ID/g), with values twice as high as those in liver and spleen (9.1 and 8.9 %ID/g, respectively). Microscopic analysis of tissue slices revealed that at 48 h post injection, 67% of intratumoral CCPM were localized extracellularly. Phenotypic analyses on the remaining 33% of intracellularly accumulated CCPM showed that predominantly F4/80$^+$ phagocytes had taken up the nanocarrier formulation. Similar uptake patterns were observed for liver and spleen. The propensity of CCPM to primarily accumulate in the extracellular space in tumors suggests that the anticancer efficacy of the formulation mainly results from sustained release of the chemotherapeutic payload in the tumor microenvironment. In addition, their high uptake by phagocytic immune cells encourages potential use for immunomodulatory anticancer therapy. Altogether, the beneficial biodistribution, efficient tumor targeting and prominent engagement of PEG-b-pHPMA-lactate-based CCPM with key cell populations underline the clinical versatility of this clinical-stage nanocarrier formulation.

1. Introduction

Nanomedicines are extensively used to improve the pharmacokinetics and biodistribution of poorly soluble or unstable drug molecules. The design of robust nanoformulations can improve their in vivo performance, resulting in improved efficacy and/or reduced side effects [1]. Various nanocarriers, such as polymer conjugates, liposomes and micelles, have been investigated over the years and several nanomedicine formulations have been approved for clinical use [2–4]. The mechanism through which nanoformulations accumulate in tumors relies on the abnormal organization of the vasculature and the lymphatic drainage system in the lesions. Nanomedicine-based drug delivery systems extravasate at sites of increased vascular permeability and are retained there because of poor lymphatics via a phenomenon described as the enhanced permeability and retention (EPR) effect [5–7].

To reach the pathological site, it is essential for nanoformulations to circulate in intact form and for prolonged periods of time. In this regard, many efforts have been made over the years to develop nanocarriers, which simultaneously provide high stability (i.e. minimal drug

* Corresponding author at: Cristal Therapeutics, Maastricht, the Netherlands.
** Corresponding authors at: Department of Nanomedicine and Theranostics, Institute for Experimental Molecular Imaging, Faculty of Medicine, RWTH Aachen University, Aachen, Germany.
E-mail addresses: cristianne.rijcken@cristaltherapeutics.com (C.J.F. Rijcken), tlammers@ukaachen.de (T. Lammers), asofias@ukaachen.de (A.M. Sofias).
[1] Equal contribution.

https://doi.org/10.1016/j.jconrel.2020.09.046
Received 11 August 2020; Received in revised form 25 September 2020; Accepted 26 September 2020
Available online 30 September 2020
0168-3659/

release prior to tumor targeting) and long circulation times in the bloodstream. An attractive platform technology enabling long-circulation properties and efficient tumor targeting is based on core-crosslinking polymeric micelles (CCPM). Several studies evaluating the performance of these CCPM as a carrier for chemotherapy have demonstrated good target site accumulation [8–10]. Long circulation half-life and improved tumor localization has for instance been reported for docetaxel-entrapped PEG-b-pHPMA-lactate-based CCPM (CPC634), which are developed by the company Cristal Therapeutics. The long circulation half-life – 16 h in rats – has contributed to the potent efficacy of this formulation against solid tumors in multiple preclinical studies. Besides, limited protein binding resulted in prolonged circulation time also in clinical patients, where CCPM reached a half-life of 39.7 h [11–14]. Clinically, the administration of CPC634 in 24 patients with solid tumors achieved 4-fold higher drug accumulation in the tumors as compared to conventional docetaxel [15]. Phase I analysis has identified 60 mg/m^2 Q3W as the maximum tolerated dose for CPC634 [14], and the formulation is currently being evaluated in phase II trial in patients with platinum-resistant ovarian cancer (NCT03742713).

Given the increasing interest in immuno-oncology, many recent studies are focusing on understanding how different nanoparticles (NPs) associate with the immune system. Analysis of the interactions between immune cells and a plethora of nanocarriers with different composition, size and ligand-decoration has led to the realization that different nanoformulations engage with different immune cell populations and that they do this to a different extent [16–18]. In this study, we investigated the biodistribution of CCPM in mice at the organism, tissue and cellular level, obtaining insights on the interaction between CCPM and "key" (immuno-modulatory) cell populations in the tumor, liver and spleen.

For investigating CCPM fate at the organism level, fluorophore-labeled CCPM were injected intravenously (i.v.) in mice bearing orthotopic 4T1 triple-negative breast cancer (TNBC) tumors, and their biodistribution and tumor accumulation were quantitatively evaluated in vivo via 3D μCT-FLT up to 48 h, and ex vivo via 2D FRI at 48 h post-injection. The CCPM displayed highly efficient tumor targeting. To investigate the localization of CCPM at the tissue and cellular level, immunofluorescence microscopy analyses were performed. In tumor, we assessed the uptake of CCPM in cancer, endothelial and immune cells. Similar analyses were performed in liver and spleen, as these organs are known to take up high amounts of NPs and have particular immunological importance. CCPM were found to accumulate extensively in F4/80$^+$ phagocytes (macrophages and Kupffer cells) in all three organs. Taken together, our result indicate that PEG-b-pHPMA-lactate-based CCPM offer multiple possibilities for targeting chemotherapeutic drugs to the tumor microenvironment and to cancer cells, as well as for the delivery of immunomodulatory compounds to immune cells.

2. Materials and methods

2.1. Synthesis and characterization of block copolymers

A block copolymer containing monomethoxy poly(ethylene glycol) (mPEG, Mn = 5000 Da) as hydrophilic block and a random copolymer of N-2-hydroxypropyl methacrylamide monolactate (HPMAmLac$_1$) and N-2-hydroxypropyl methacrylamide dilactate (HPMAmLac$_2$) as thermosensitive block (approx. Mw 7500 Da) was synthesized by free radical polymerization using (mPEG$_{5000}$)$_2$-ABCPA as initiator [9]. The HPMAmLac$_1$/Lac$_2$ comonomer feed ratio was 25/75 (mol/mol) and the ratio of initiator/monomer was 1/20 (mol/mol). In brief, HPMAmLac$_1$ (4.65 mmol,1.00 g), HPMAmLac$_2$ (13.95 mmol, 4.00 g) and (mPEG$_{5000}$)$_2$-ABCPA initiator (0.93 mmol, 9.30 g) were dissolved in acetonitrile (32 ml) in a round bottom flask. The reaction mixture was flushed with nitrogen for at least 15 min, heated to 70 °C and then stirred for 24 h. Next, the resulting block copolymer was precipitated by dropwise adding the reaction mixture into an excess of diethyl ether (260 ml). The precipitate was filtered and dried in a vacuum oven overnight to obtain mPEG$_{5000}$-*b*-pHPAMmLac$_n$ (n = 1 or 2) block copolymer as off-white solids. Next, a fraction (10 mol%) of the block copolymer lactate side chains was derivatized with 2-(2-(methacryloyloxy)-ethylsulfinyl)acetic acid (referred to as "L2") via a pivalic anhydride intermediate [19] to obtain L2-derivatized block copolymer following a previously reported protocol [12]. Analytical characterization by NMR, GPC and UV–Visible spectroscopy [12] revealed that the obtained L2-derivatised mPEG$_{5000}$-*b*-pHPAMmLac$_n$ (n = 1 or 2) block copolymer (purity > 85%) has a M$_n$ of 7.5 kDa, with the same comonomer ratio as in feed (i.e. HPMAmLac$_1$/Lac$_2$ = 25/75, mol/mol) and a critical micelle temperature of 10 °C.

Similarly, a block copolymer with azide functionalization on the PEG terminus was synthesized following the same protocol [9], except that azide-PEG$_{5000}$-OH (Celares GmbH, Germany) was used as the starting material to synthesize corresponding initiator and resulting (L2-derivatized) block copolymers instead of mPEG$_{5000}$-OH. The generated L2-derivatised azide-PEG$_{5000}$-*b*-pHPAMmLac$_n$ (n = 1 or 2) block copolymer (purity > 85%) also has a M$_n$ of 7.5 kDa, with the same comonomer ratio (i.e. HPMAmLac$_1$/Lac$_2$ = 25/75, mol/mol) and critical micelle temperature (i.e. 10 °C).

2.2. Preparation of azide-functionalized core-crosslinked polymeric micelles

Azide-functionalized CCPM were manufactured essentially following the reported protocol [12]. In brief, an ice-cold aqueous solution of L2-derivatized mPEG$_{5000}$-*b*-pHPAMmLac$_n$ block copolymer (78.85 v %, 24.1 mg/ml) and L2-derivatized azide-PEG$_{5000}$-*b*-pHPAMmLac$_n$ block copolymer (4.15 v%, 24.1 mg/ml) were mixed with TEMED (2.5 v%, 120 mg/ml) dissolved in 150 mM ammonium acetate pH 5.0 buffer. Subsequently, absolute ethanol (10 v%) was added dropwise to the mixture, followed by rapid heating to 60 °C while stirring vigorously for 1 min to form polymeric micelles. The micellar dispersion was then transferred into an airtight vial containing KPS (4.5 v%, 30 mg/ml) dissolved in 150 mM ammonium acetate pH 5.0 buffer at room temperature. The polymeric micelles were covalently stabilized by polymerization of the methacrylate moieties on the block polymer in N$_2$ atmosphere at room temperature for 1 h, generating azide-functionalized CCPM. The obtained micellar dispersion was filtered through a 0.2 μm cellulose membrane filter to remove potential aggregates. Next, azide-functionalized CCPM were purified in isotonic 20 mM phosphate pH 7.4 buffer containing NaCl and concentrated to 50 mg/ml polymer equiv. by means of Tangential Flow Filtration (TFF) equipped with a modified Polyethersulfone (mPES) 100 kDa module (Spectrumlabs).

2.3. Synthesis of cyanine 7-labeled core-crosslinked polymeric micelles

Cyanine 7 (Cy7)-labeled CCPM were synthesized by conjugating Cy7-BCN fluorescent dye to the surface of azide-functionalized CCPM via copper-free click chemistry (Fig. S1). Cy7-BCN was conjugated to azide-functionalized CCPM by mixing 0.463 μmol Cy7-BCN (stock solution in DMSO) with CCPM containing 0.925 μmol azide equiv. The reaction mixture was stirred in the dark at room temperature overnight. The progress of the conjugation was controlled by monitoring the content of remaining Cy7-BCN in the reaction using UPLC-UV (see Supplementary Methods), while > 95% content recovery of Cy7-BCN control under the reaction condition (i.e. dissolved in DMSO/phosphate buffer mixture, but without addition of azide-functionalized CCPM) had been confirmed assuring Cy7-BCN stability during reaction. The conjugation reaction was stopped after 16 h when 20% of fed Cy7-BCN was consumed in the click reaction, generating Cy7-labeled CCPM in which 0.5 w% of polymer chains was covalently attached by a Cy7 label. The obtained Cy7-labeled CCPM was purified by TFF against 15 v% ethanol to remove unreacted Cy7-BCN label, followed by buffer swap into isotonic 20 mM phosphate pH 7.4 buffer containing NaCl. The resulting Cy7-labeled CCPM test item contains 50 mg/ml polymer equiv. as

quantified by UPLC-UV [13] and 33 μM Cy7 equiv. based on conjugation conversion, and has a hydrodynamic diameter of 50 nm as determined by dynamic light scattering (PDI ≤ 0.2).

2.4. In vitro and in vivo models

4T1 breast cancer cells (American Type Culture Collection, Manassas, VA, USA) were cultured in RPMI medium (RPMI 1640; Gibco, Life Technologies GmbH, Germany), supplemented with 10% fetal bovine serum (FBS; Life Technologies GmbH, Germany) and 1% penicillin/streptomycin (10,000 U/ml penicillin; 10 mg/ml streptomycin, Life Technologies GmbH, Germany), at 37 °C and 5% CO_2 in a humid atmosphere. All animal experiments were approved by local and institutional ethical committees. Six- to eight-weeks old BALB/cAnNRj female mice (Janvier Labs, France) were kept in pathogen-free cages with food and water ad-libitum, a light/dark cycle of 12/12 h and separate ventilation. 4T1 breast cancer cells (2.5×10^4) were orthotopically inoculated into the right abdominal mammary gland fat pad of the mice and the tumors were allowed to grow for 10 days, until they reached a size of approximately 5 mm in diameter. The size of the tumors was monitored daily. Seven days before starting the in vivo experiments, the mouse diet was switched to chlorophyll-free food, to reduce background signals during optical imaging.

2.5. μCT-FLT imaging

For all in vivo experiments, anesthesia was induced using 4% isoflurane (Forene, Abbott, Wiesbaden, Germany) in oxygen-enriched air using a dedicated vaporizer. During imaging, the isoflurane concentration was reduced to 2.0% and maintained on this level. Eyes were protected from desiccation with Bepanthen eye ointment (Bayer Vital GmbH, Germany). For intravenous injection, a sterile catheter prepared by connecting a 30 G cannula (B.Braun, Melsungen, Germany) to a polyethylene tube (inner diameter of 0.28 mm and outer diameter of 0.61 mm, wall thickness of 0.165 mm (Hartenstein, Würzburg, Germany)) was inserted into the lateral tail vein of the mice. Mice were randomly divided in two groups and injected either with Cy7 as a free dye or with Cy7-labeled CCPM (2 nmol; in 50 μl 0,9% NaCl sterile solution). The in vivo biodistribution of free dye and CCPM was imaged using a hybrid micro-computed tomography-fluorescence tomography (μCT-FLT) device (U-CT OI, MILabs B.V., Utrecht, the Netherlands). Anesthetized mice were placed between two acrylic glass plates in the animal holder, positioned between the FLT laser and the cooled CCD camera. Approximately 130 scan points were acquired using a laser and filter with excitation and emission wavelengths at 730 and 775 nm, respectively. After acquiring the FLT scan, the animal holder was automatically moved to the CT to acquire a total body scan for the anatomic localization of the regions of interest. In a full-rotation in step-and-shoot mode, 480 projections (1944 × 1536 pixels) were acquired with an x-ray tube voltage of 55 kV, power 0.17 mA and exposure time of 75 ms. This procedure was followed for each mouse right before the i.v. injection of free dye or CCPM and at 0.25, 4, 24 and 48 h post-injection, to longitudinally visualize the fluorescence signal accumulation in different organs. After the last μCT-FLT scan, the animals were sacrificed and organs were excised for ex vivo evaluation. The harvested organs were imaged using a fluorescence molecular tomography device (FMT 400, PerkinElmer, Waltham, MA, USA) in 2D reflectance imaging mode at 750 nm excitation wavelength. Tissues were finally embedded in TissueTek O.C.T. (Sakura Finetek Europe, the Netherlands) and preserved at −80 °C.

2.6. μCT-FLT and FRI image analysis

All acquired 3D CT images were reconstructed at an isotropic voxel size of 80 μm using a Feldkamp type algorithm (filtered back-projection). Shape, scattering maps and absorption maps were automatically generated and used for 3D fluorescence reconstruction [20]. 3D organ segmentations were generated based on the μCT data using interactive segmentation operations (Imalytics Preclinical, Gremse-IT GmbH, Aachen, Germany) according to a previously optimized protocol [21,22]. Segmentations of heart, lungs, liver, spleen, kidneys, bone and spinal marrow, bladder and tumor were generated for all mice at all time-points post-injection. The fluorescence signal acquired in the total body FLT scans at 0.25 h after injection was used to generate a scale factor for calibration and the concentrations (in %ID/g) were computed by assuming a density of 1 g/cm^3 [23]. Means and standard deviations were computed based on multiple mice for each region (e.g. tumor), time point and probe.

2.7. Cellular uptake of CCPM in tumor, liver and spleen

Fluorescence microscopy (Axio Imager M2 microscopy system, Carl Zeiss, Göttingen, Germany) was applied to DAPI stained cryosections (n = 5 images per section) from tumor, liver and spleen. Afterwards, tissue sections were fixed with methanol 80% and −20 °C acetone, and washed three times with PBS (Life Technology, Germany). Via the fixation and washing steps, extracellularly localized micelles were removed. Fluorescence images were captured at exactly identical locations. The signal of the micelles was quantified using AxioVision SE64 Rel. 4.8 software (Carl Zeiss, Jena, Germany) and compared between both pre- and post-washing images. The data obtained as percentage of area fraction was plotted as average ± standard deviation in GraphPad Prism 8 (GraphPad Software, USA).

2.8. Cellular localization of CCPM in tumor, liver and spleen

Immunohistochemical stainings were performed on 8 μm-thick cryosections. A standard protocol was applied for the staining of tumor, liver and spleen. The slices were first fixed with methanol 80% and −20 °C acetone, then washed with PBS, and then incubated for one hour with two antibodies at the same time for each set of stainings. Tumors were incubated with a combination of anti-CD31 antibody (1:50) (Acris, Germany) and either anti-F4/80 antibody (1:50) (Bio-Rad, Germany) or anti-CD45 antibody (1:200) (Cell Signaling, Germany), diluted in 12% BSA/PBS (PAN Biotech, Germany). Livers were co-stained with anti-CLEC4F antibody (1:20) (Bio-Techne, Germany) and anti-F4/80 antibody (1:50) (Bio-Rad, Germany), or anti-CD31 antibody (1:50) (Acris, Germany) and anti-HNF4α antibody (1:200) (Abcam, UK), diluted in 12% BSA/PBS. Spleens were co-stained with BSA-diluted anti-CD31 antibody (1:50) (Acris, Germany) and either anti-F4/80 antibody (1:50) (Bio-Rad, Germany) or anti-CD45 antibody (1:200) (Cell Signaling, Germany); in another set of stainings, the anti-CD45 antibody (1:200) was combined with an anti-CD11b antibody (1:500) (Thermo Fisher, USA). After three PBS washing steps, samples were incubated for 45 min with the corresponding secondary antibodies diluted in 12% BSA/PBS: Cy3 anti-Rat (1:500), Alexa Fluor 488 anti-Rabbit (1:500), Cy3 anti-Rabbit (1:500), Alexa Fluor 488 anti-Rat (1:350), Alexa Fluor 488 anti-Goat (1:500), Cy3 anti-Mouse (1:150) (Dianova, Germany), as well as with DAPI (1:500) (Merck, Germany). The slides were then again washed with PBS, mounted with Mowiol 4–88 (Carl-Roth, Germany) and glass-covered. A slightly different protocol was used for the co-staining of CD45 and CD31 in the liver: liver sections were fixed in paraformaldehyde (PFA) 4%, washed with PBS/azide solution (in a ratio 0.2/1 g/l) and blocked with 2% BSA diluted in PBS/azide for 10 min. The slices were then incubated for 1 h with anti-CD45 antibody (1:100) (Bio-Techne, Germany) and anti-CD31 antibody (1:50) diluted in a PBS/azide solution added with 1% mouse serum (Sigma-Aldrich, Germany). After washing with PBS/azide, the slices were blocked again with 0.2% BSA diluted in PBS/azide for 5 min. The corresponding secondary antibodies [Cy3 anti-Rat (1:500) and Alexa Fluor 488 anti-Rabbit (1:500)] together with DAPI (1:500) were diluted in 1% mouse serum diluted in PBS/azide and applied to

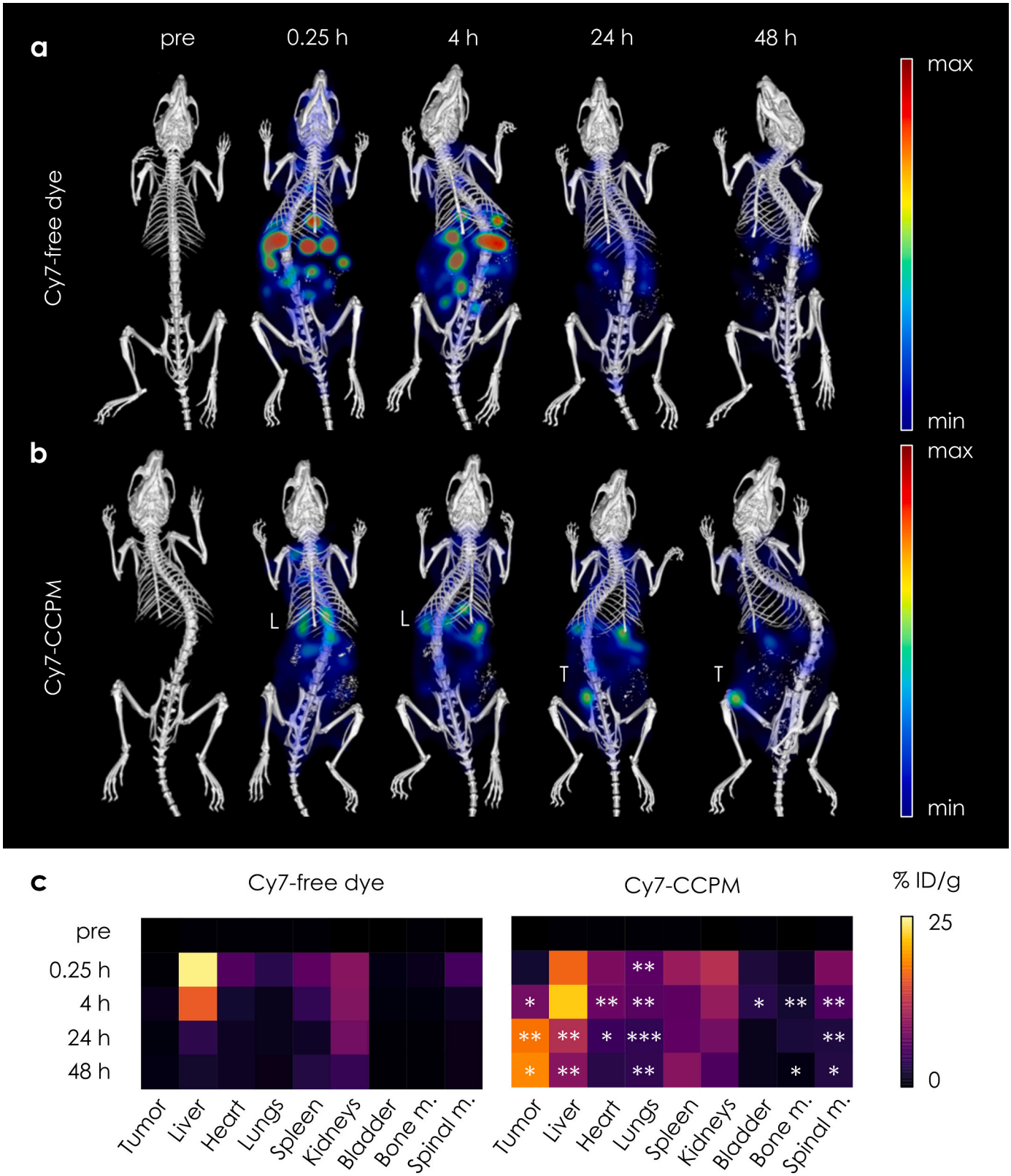

Fig. 1. CCPM efficiently target tumors in vivo. (a) By means of 3D μCT-FLT imaging, it is shown that Cy7 administered as a free dye is rapidly cleared through liver and kidneys, resulting in very low accumulation in 4T1 tumors in mice. Free Cy7 is almost entirely cleared after 48 h. (b) The long circulation properties of CCPM and their relatively low localization in clearance organs enabled strong and specific accumulation in 4T1 tumors over time. (c) Heat-maps comparing the biodistribution profiles between free Cy7 and Cy7-CCPM. CCPM show prolonged accumulation and therefore efficacious targeting to tumors (these heat-maps are based on the data provided in Fig. S2). *P* values: * < 0.05, ** < 0.01, *** < 0.001.

the sections for 45 min. The samples were washed at first with PBS/azide, subsequently with water, and then mounted with Mowiol 4–88 to enable glass-covering. Images of all stained slides were acquired using fluorescence microscopy. Eight representative images were acquired per section and the area fraction of the signals was quantified using the AxioVision SE64 Rel. 4.8 software. Images were further analyzed with Inform software (PerkinElmer, USA) to evaluate the co-localization of cells with micelles. All cells were first segmented and then phenotyped using CD45, CD31, F4/80, HNF4α, CLECF4 and CD11b. Separate setups were applied for the analysis of the CCPM association with each marker studied. Four categories resulted from the processing of each image: single positivity of the cell for the marker, single positivity for CCPM, double positivity for marker and CCPM, and double negativity. For each cell subpopulation, we calculated the ratio of $CCPM^+$ cells over the total cells. Based on these numbers, the distribution pattern of CCPM at the cell level was calculated. All values obtained were plotted as averages in pie charts using the GraphPad Prism 8 software.

2.9. Statistical analysis

The data from the μCT-FLT analyses, FRI scans and cellular uptake studies were analyzed via the unpaired two-tailed *t*-test (GraphPad Prism 8 software). Significant differences were considered for p values < 0.05 (*), $p < 0.01$ (**) and $p < 0.001$ (***).

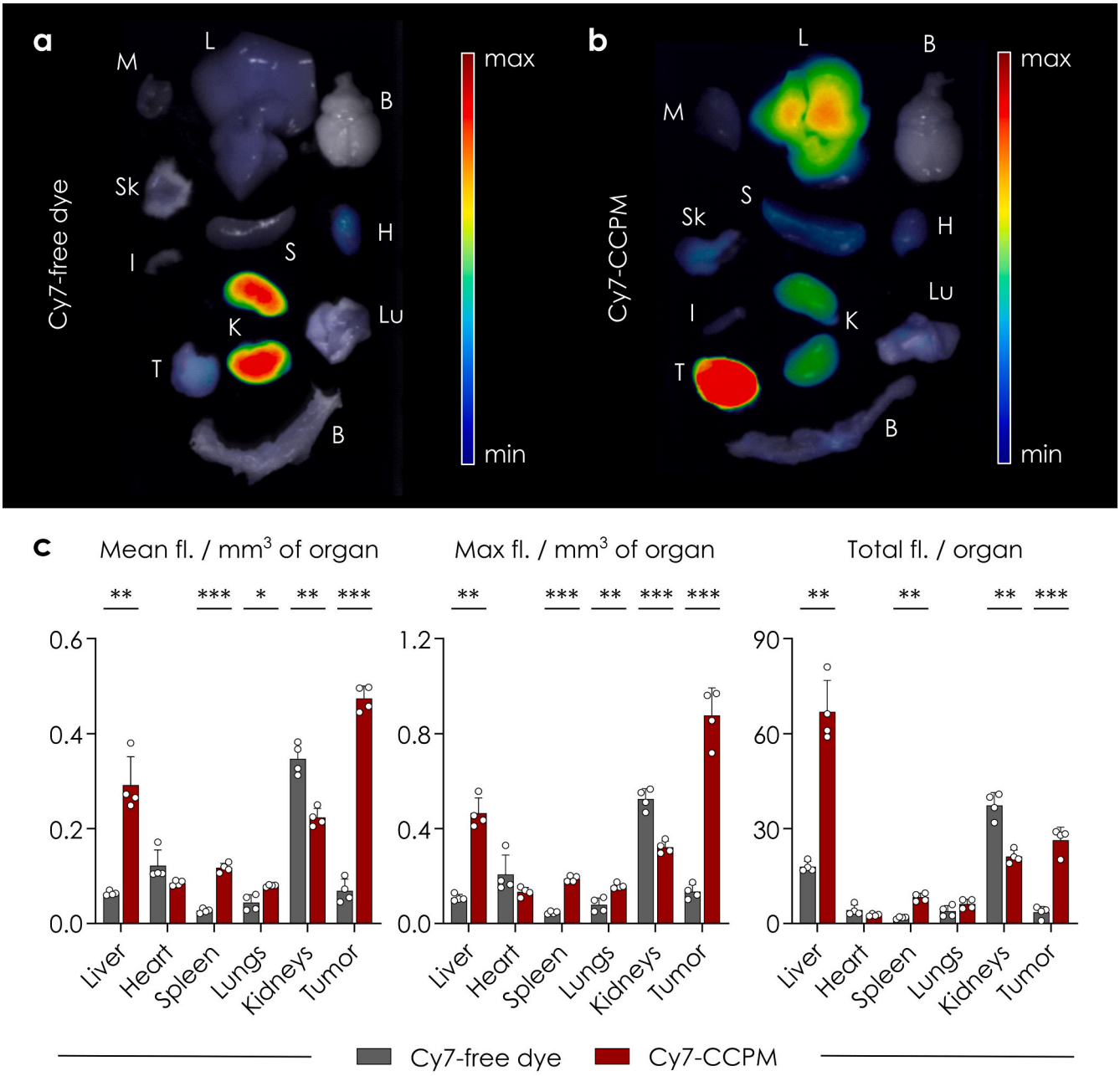

Fig. 2. Ex vivo organ analysis confirms the efficient tumor accumulation of CCPM. (a) 2D fluorescence reflectance imaging (FRI) of resected organs at 48 h post i.v. administration shows high levels of free Cy7 in the kidneys. M = muscle, L = liver, B = brain, Sk = skin, S = spleen, H = heart, I = intestine, K = kidneys, Lu = lung, T = tumor, B = bone marrow. (b) The strongest FRI signals for Cy7-labeled CCPM were observed for tumor. (c) Quantification of the ex vivo organ fluorescence for free Cy7 and Cy7-labeled CCPM. P values: * < 0.05, ** < 0.01, *** < 0.001.

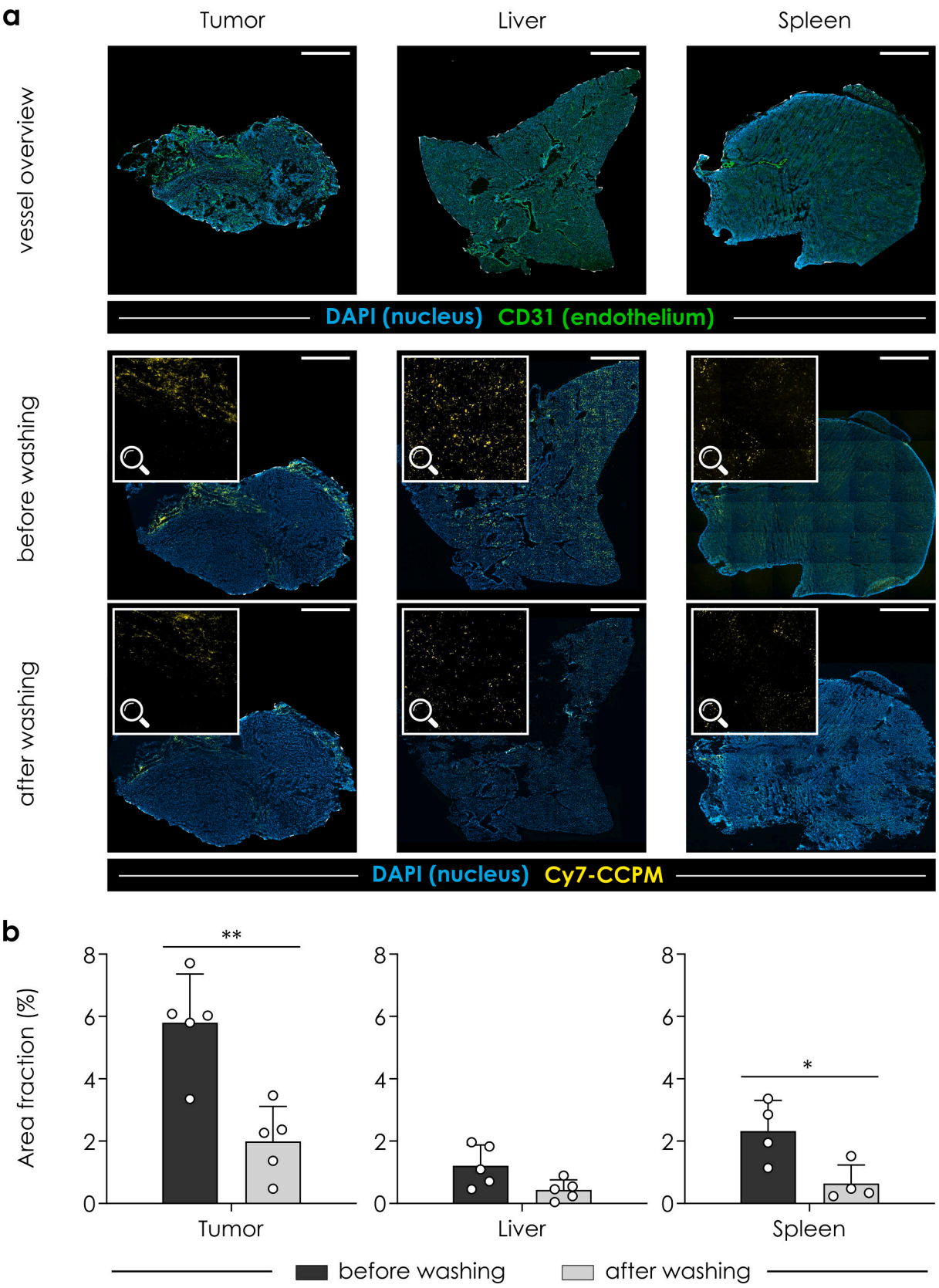

Fig. 3. CCPM mainly accumulates extracellularly in tumor, liver and spleen. (a) Fluorescence microscopy images showing $CD31^+$ vasculature in tumor, liver and spleen. Vessels appear homogeneous in liver and spleen, but are heterogeneously distributed in tumor. CCPM localization is in accordance with the vessel distribution. Magnifications show CCPM accumulation before and after washing with PBS. This "washing" step exemplifies that most CCPM locate extracellularly. Scale bar = 1000 μm. (b) Quantification of CCPM in tumor, liver and spleen before and after washing, showing that approximately 2/3 of the CCPM remains extracellularly while only a third is taken up by cells. *P* values: * < 0.05, ** < 0.01.

3. Results

3.1. CCPM distribution at the whole-body level

The biodistribution of Cy7-labeled CCPM after i.v. administration into mice bearing 4T1 tumors was assessed in vivo via 3D μCT-FLT (free Cy7 dye was injected as a low-molecular-weight control). As anticipated, at early time points post-injection (i.e. at 0.25 and 4 h), the free dye accumulated in the clearance organs (liver, kidneys) and consequently very low levels of the dye reached tumors (Fig. 1a). In contrast, the Cy7-CCPM displayed a totally different biodistribution profile with low retention by liver and high tumor targeting to be observable at 24 and 48 h post-injection (Fig. 1b). Quantitative full-biodistribution analysis at the organ level at various time points revealed that the free dye was eliminated very rapidly from the body. Kidneys and liver contained the highest amount of free dye, indicative of the hepatic and renal clearance that small molecules typically undergo, while only insignificant tumor targeting was achieved (0.7 %ID/g) (Fig. 1c and Fig. S2). Conversely, the CCPM achieved a very high tumor localization. In line with EPR-mediated tumor accumulation, the concentration of CCPM in tumors progressively increased over time: 2.1 %ID/g at 0.25 h, 7.9 %ID/g at 4 h, 17.4 %ID/g at 24 h, and 18.6 %ID/g at 48 h (Fig. 1c and Fig. S2). At the latest time-point, CCPM uptake by liver and spleen was 50% lower than in tumors, i.e. 9.1 and 8.9 %ID/g respectively (Fig. 1c and Fig. S2). Besides tumor, liver and spleen, the CCPM also accumulated in lungs and in (spinal) bone marrow (Fig. 1c and Fig. S2). At the whole-body level, the amount of free Cy7 still present in the mice at 48 h post-injection was found to be 19.7 %ID/g, as compared to 65.9

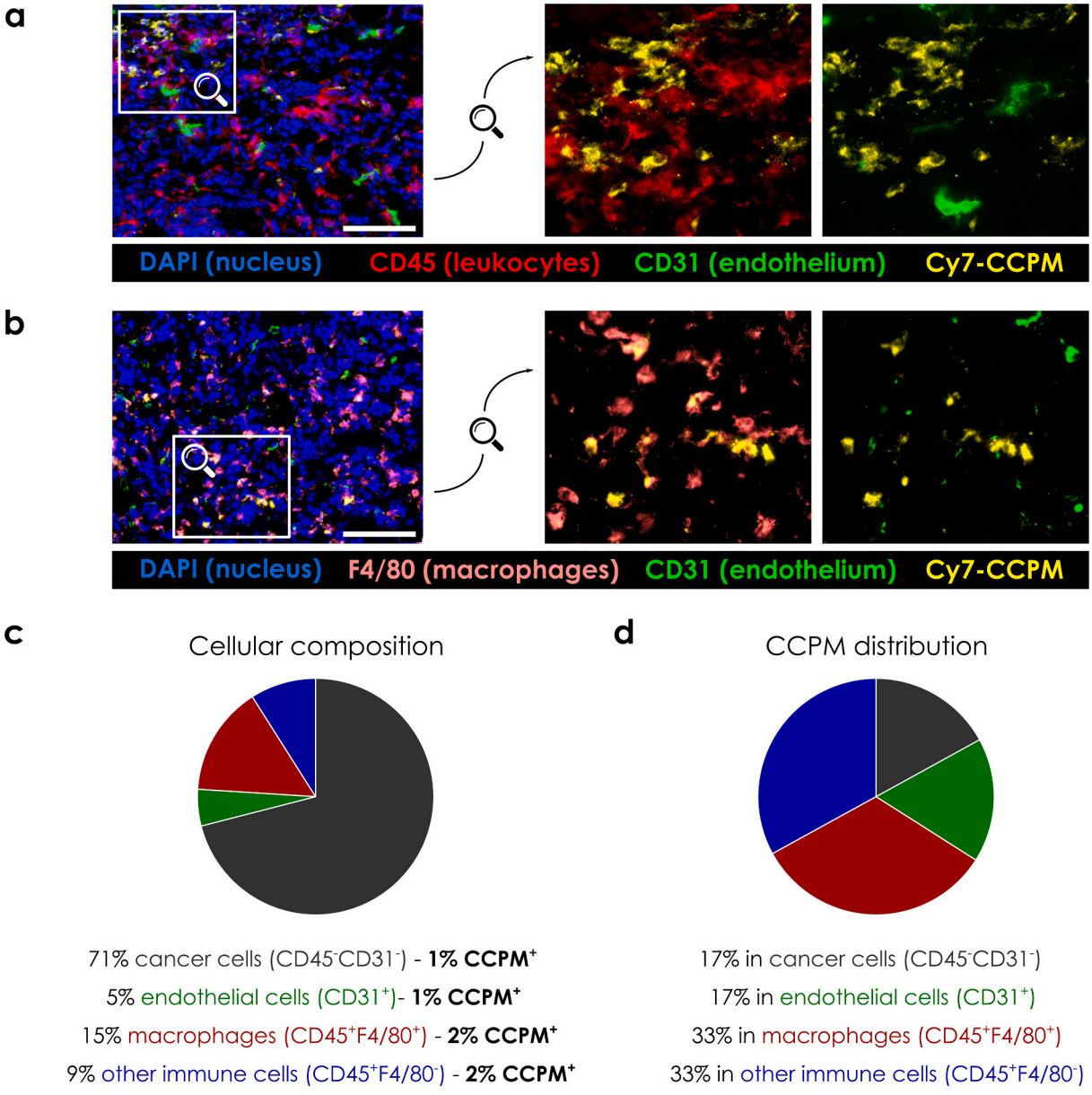

Fig. 4. CCPM uptake by tumor-associated cell populations. (a) Fluorescence microscopy images of leukocytes and endothelial cells in tumors. The enlarged images reveal strong uptake of CCPM in leukocytes and low uptake in endothelial cells. Scale bar = 100 μm. (b) F4/80 and CD31 stainings show strong uptake of CCPM by F4/80$^+$ tumor-associated macrophages. Scale bar = 100 μm. (c) Pie chart representing cellular composition in tumor. Cancer cells make 71% of the total mass, leukocytes 24% (15% of which are macrophages), and endothelial cells 5%. As shown in bold text next to each cell type, 1/71 cancer cells, 1/5 endothelial cells, 2/15 macrophages, and 2/9 other immune cells were found to be CCPM positive. (d) Pie chart shows the distribution of the intracellular CCPM within different cell types. Most CCPM (66%) in tumors are phagocytosed by immune cells; especially macrophages (33%). The rest of the CCPM found to distribute equally between cancer cells and endothelial cells (17% for each).

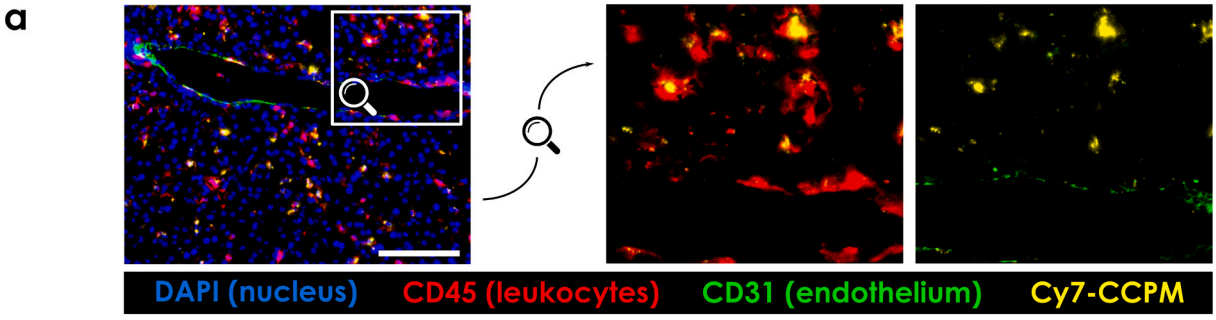

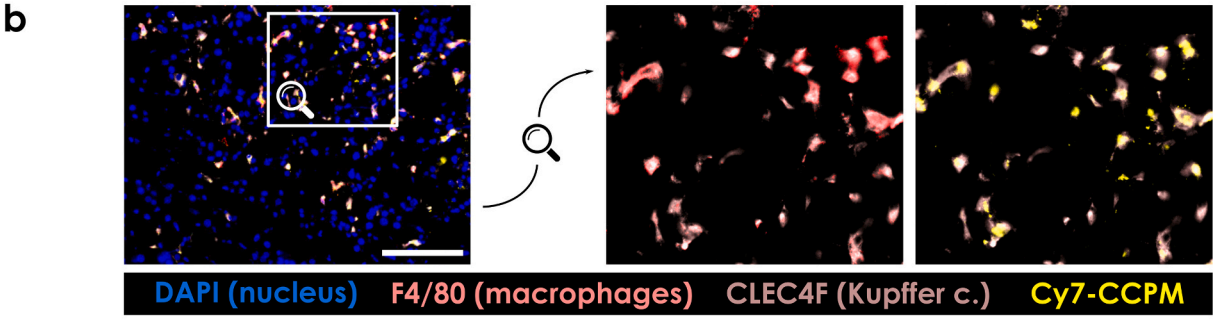

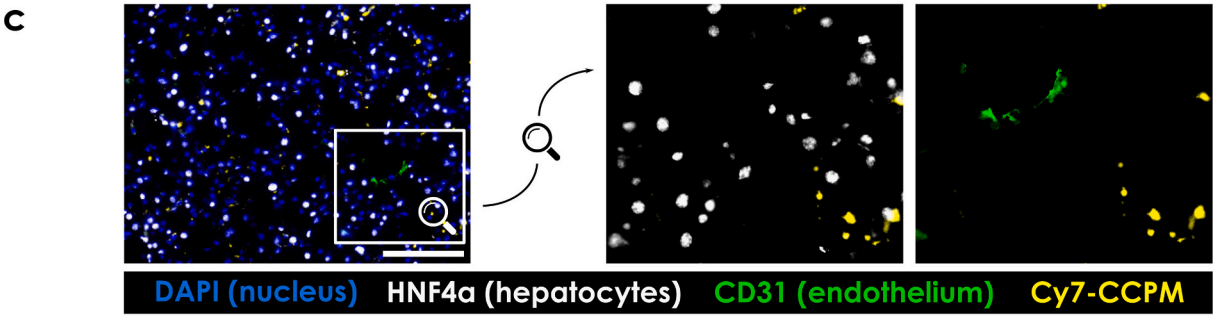

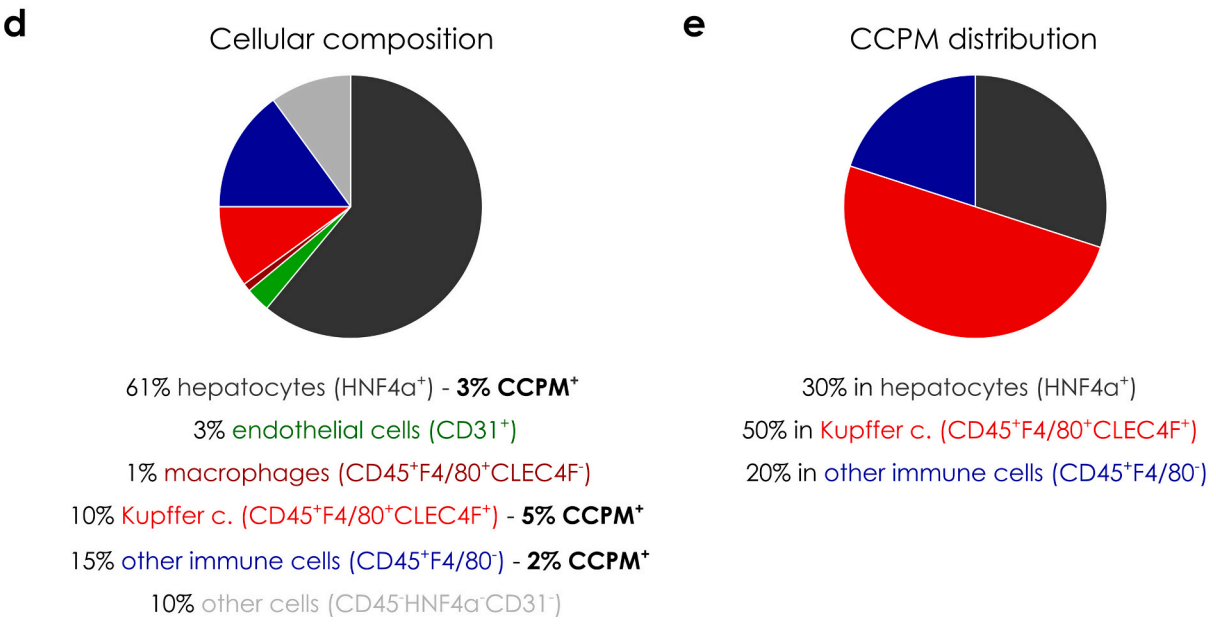

(caption on next page)

Fig. 5. CCPM uptake by different cell populations in liver. (a) Fluorescence microscopy images and endothelial cells in the liver. The enlarged images show strong association of CCPM with leukocytes and low association with endothelial cells. Scale bar = 100 μm. (b) Fluorescence microscopy images of macrophages and Kupffer cells, exemplifying that 90% of liver macrophages are Kupffer cells and showing strong uptake of CCPM by Kupffer cells. Scale bar = 100 μm. (c) Fluorescence microscopy images of hepatocytes and endothelial cells in the liver, showing low association of CCPM with both hepatocytes and endothelial cells. Scale bar = 100 μm. (d) Pie chart displaying the cellular composition of the liver: 61% of the cells are hepatocytes, 26% immune cells (of which 10% are Kupffer cells, 1% macrophages, and 15% other immune cells), 3% endothelial cells and the remaining 10% other cells. As shown in bold text next to each cell type, 3/61 hepatocytes, 5/10 Kupffer cells and 2/15 other immune cells were found to be CCPM positive. (e) Pie chart displaying the distribution of intracellular CCPM within different cell types in the liver, showing that 50% is taken up by Kupffer cells, 20% by other immune cells and 30% by hepatocytes.

%ID/g for Cy7-CCPM (Fig. S3), which exemplifies that nanocarriers delay the clearance of small molecules from the body.

To validate the μCT-FLT data, tumors and healthy tissues were collected after sacrificing the animals at 48 h post-injection, and the Cy7-derived fluorescence signals were assessed for each tissue via 2D FRI. In good agreement with in vivo data, ex vivo analysis showed the free dye to be predominantly present in the kidneys, while insignificant amounts of fluorescence were detectable in other tissues (Fig. 2a). The ex vivo imaging of organs from mice that were injected with CCPM were also in good agreement with the in vivo data, with the tumors showing the strongest fluorescence signals (Fig. 2b). The ex vivo analysis revealed a comparable biodistribution pattern as the in vivo analysis, with apart from tumor most nanoparticle signals coming from liver, spleen and kidney (Fig. 2c). Overall, as evident from in vivo and ex vivo analysis (Figs. 1, 2 and Fig. S2), CCPM exhibit a beneficial biodistribution profile with high tumor accumulation, with a certain level of retention in organs of the mononuclear phagocytic system (i.e. liver and spleen), and with low concentrations in the majority of other organs.

3.2. CCPM distribution at the tissue level

Since the assessment of CCPM biodistribution at the organism level revealed that the nanocarrier predominantly accumulates in tumor, liver and spleen, the CCPM tissue distribution was analyzed specifically in these three organs. As expected, liver and spleen were highly vascularized and the vessels were homogenously distributed all over the tissue. In contrast, tumors, known to be highly chaotic with regard to blood vessel distribution and microenvironment composition, displayed a heterogeneous vessel distribution. In line with the vasculature distribution, we observed that CCPM were homogeneously distributed in the liver and spleen, whereas localization in tumors was highly heterogeneous, as evidenced by clustered fluorescence (Fig. 3a). Despite the fact that tumor accumulation was heterogeneous, larger area fractions were positive for CCPM in tumors than in liver and spleen. More specifically, 5.8% of the total tumor area was CCPM-positive, as compared to 1.2% and 2.3% for liver and spleen, respectively (Fig. 3b). Via adding a washing step in the protocol, the extracellularly localized CCPM were removed, enabling the assessment (relative quantification) of the intracellularly localized CCPM. After this step, CCPM were still present in tumor, liver, and spleen, covering a 2%, 0.4%, and 0.6% of the area fraction for each organ respectively (Fig. 3b). Comparing the Cy7 signal in the extracellular versus the intracellular compartment, it appeared that approximately 2/3 of the material was localized extracellularly at 48 h post injection, for all three tissues analyzed (65.7% for tumor, 64.1% for liver and 72.4% for spleen; Fig. 3a,b). This non-internalized fraction of CCPM may contribute to the anticancer activity upon the prolonged release of the drug to the surrounding tumor microenvironment. These findings extend the efficient tumor accumulation of CCPM observed at the organism level, towards a more detailed insight into the tissue distribution and cellular internalization levels.

3.3. CCPM distribution at the cellular level

Because a considerable amount (33%) of CCPM was localized intracellularly in tumor, liver and spleen, we subsequently set out to study which cells are responsible for engaging with the CCPM. Since F4/80-positive phagocytes are involved in taking up nanomaterials in several tissues (e.g. $F4/80^+Ly6C^-$ M2-like macrophages in tumor, $F4/80^+CLEC4F^+$ Kupffer cells in liver, and $F4/80^+$ macrophages in spleen [24–26]), we paid particular attention to analyzing CCPM co-localization with these cells. Additionally, since emerging evidence indicates that NP enter tumors via endothelial transcytosis, we also studied the internalization of CCPM by CD31-positive endothelial cells [27]. Multiple different stainings were performed on 4T1 tumor slices, showing high levels of CCPM in the tumor microenvironment and co-localization with $CD45^+$ leukocytes, with $CD45^+F4/80^+$ macrophages and with $CD31^+$ endothelial cells (Fig. 4a,b). Cellular profiling of tumor composition showed that 71% of the cancerous mass can be attributed to cancer cells ($CD45^-CD31^-$), 24% to leukocytes ($CD45^+$) and 5% to endothelial cells ($CD31^+$). Among all $CD45^+$ leukocytes, macrophages accounted for 62%, complying with the notion that the majority of immune cells in the tumor microenvironment are macrophages (Fig. 4c). We next analyzed the CCPM uptake within the different cell populations. Of all intracellularly localized CCPM, 66% was found to be inside $CD45^+$ leukocytes. A smaller fraction was internalized by $CD45^-CD31^-$ cancer cells and by $CD31^+$ endothelial cells (Fig. 4d). Of note, even though immune cells made only 24% of all cells present within the tumor, they were responsible for endocytosing 66% of the total intracellular CCPM, exemplifying the high propensity of these cells to take up nanoparticles.

Histological analyses of liver sections showed that CCPM co-localized with cells positive for CD45, F4/80, CLEC4F and HNF4a markers, indicating nanoparticle uptake by leukocytes, macrophages, Kupffer cells and hepatocytes, respectively (Fig. 5a,b,c). Surprisingly, in contrast with observations in tumors, no co-localization between endothelial cells ($CD31^+$) and CCPM was observed (Fig. 5a,c). Liver cell profiling showed 61% of total liver-residual cells to be $HNF4a^+$ hepatocytes, 26% to be leukocytes (among which 10% were Kupffer cells), and 3% endothelial cells (Fig. 5d). Analysis of nanocarrier uptake showed that 50% of intracellularly localized CCPM in the liver was endocytosed by Kupffer cells (Fig. 5e). The other half CCPM amount was distributed in hepatocytes (30%) and other $CD45^+$ immune cells (20%). Comparable to the pattern observed in tumor, the relatively small immune cell fraction (26% of all cells in the liver) was responsible for taking up the vast majority of CCPM (70%), underlining the strong association between the nanoparticles and immune cells.

In line with tumor and liver, also in spleen CCPM predominantly co-localized with cells positive in leukocyte markers (CD45, CD11b, and F4/80) and insignificantly with endothelial cells (Fig. 6a,b,c). In line with the knowledge that the spleen is an important compartment for the immune system, the vast majority of the cell population in spleen appeared indeed to be immune cells, which accounted for 67% of the total cells. Only 1% of the total cells was represented by endothelial cells ($CD31^+$), and the rest 32% by other $CD45^-$ splenocytes ($CD45^-CD31^-$). Comparing the immune cell major sub-populations, we identified higher amount of myeloid than lymphoid cells (39% vs 28%) (Fig. 6d). Half of the total endocytosed CCPM in the spleen were detected in macrophages. The remaining CCPM ended up in lymphoid cells (27%) or in other cells (23%) (Fig. 6e).

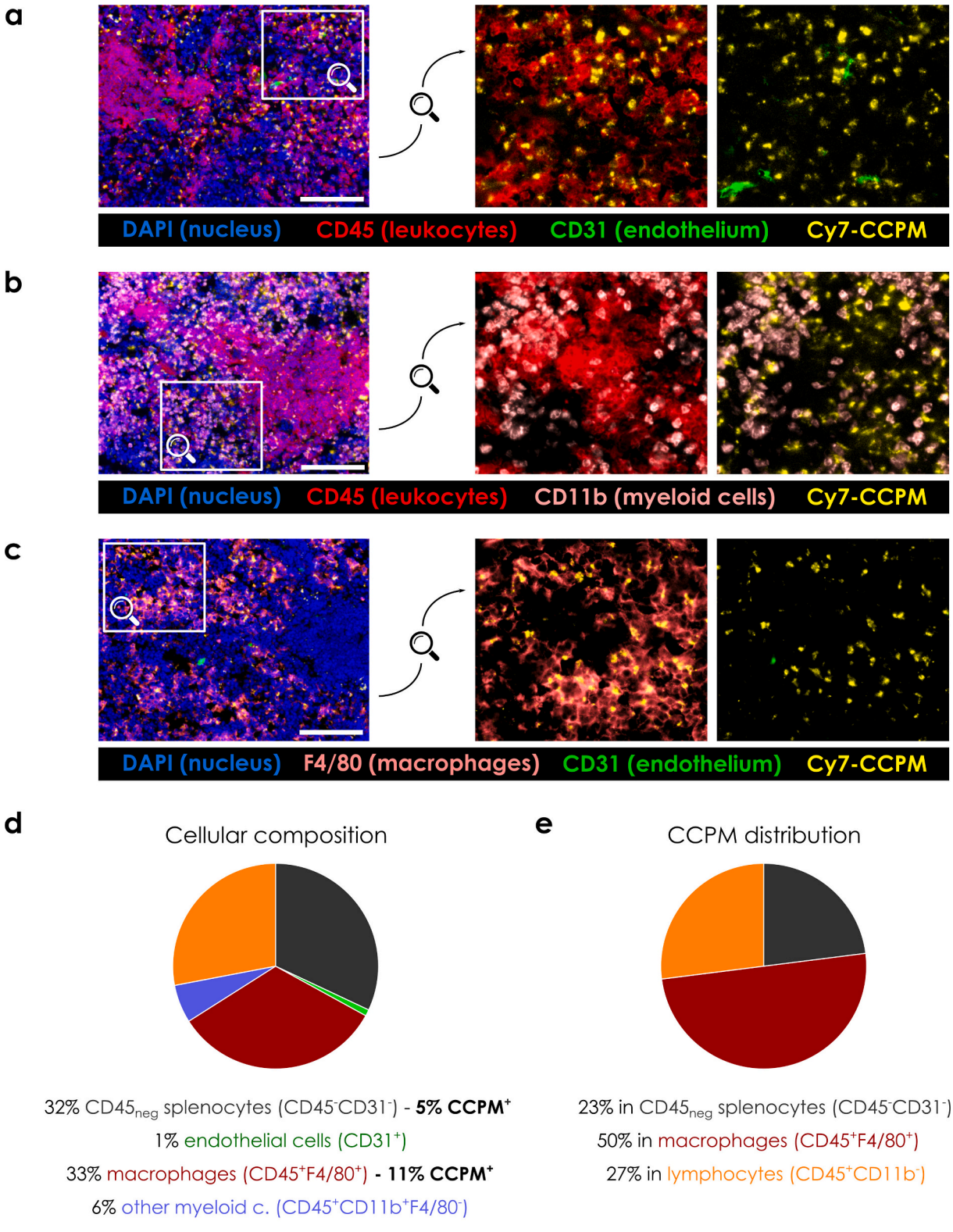

Fig. 6. CCPM uptake by different cell populations in spleen (a) Fluorescence microscopy images and endothelial cells in the spleen. The enlarged images show high association of CCPM with leukocytes and minor association with endothelial cells. Scale bar = 100 μm. (b) Representative image of leukocytes and myeloid cells, exemplifying that more than half of all splenic immune cells are myeloid cells and that CCPM strongly associate with these cells. Scale bar = 100 μm. (c) Fluorescence microscopy images of macrophages and endothelial cells in the spleen, showing strong CCPM uptake by macrophages. Scale bar = 100 μm. (d) Pie chart displaying the cellular composition of the spleen: 67% of the splenic mass is composed of leukocytes (33% are macrophages, 28% lymphocytes and 6% other myeloid cells), 1% of endothelial cells and 32% of $CD45^-$ splenocytes. As shown in bold next to each cell type, 11/33 macrophages, 6/28 lymphocytes and 5/32 $CD45^-$ splenocytes are CCPM positive. (e) Pie chart displaying the distribution of intracellular CCPM within different cell types in the spleen, showing that 50% is taken up by macrophages, 27% by lymphocytes and 23% by other cells.

4. Discussion

In this study, we investigated the localization of clinical-stage CCPM at the whole-body, tissue and cellular level. This multi-scale analysis revealed high tumor accumulation for fluorophore-labeled CCPM, as well as extensive engagement with phagocytic immune cells in tumor, liver and spleen. The mapping of CCPM biodistribution after i.v. administration contributes to better understanding of its potent in vivo anticancer performance, and it provides important new insights with regard to exploring the potential of CCPM for immunomodulatory anticancer therapy.

Recent studies analyzing CCPM pharmacokinetics in rats found a prolonged circulation half-life time of 16 h, as well as a negligible formation of a protein corona [11]. The protein corona determines the in vivo fate of nanomedicine formulations; strong NP surface coverage with opsonizing proteins typically results in rapid and strong recognition by circulating phagocytes, as well as by liver and spleen, reducing the formulations' half-life times in blood [28,29]. In the case of CCPM, it seems that negligible protein corona formation plays a key role in bypassing uptake by circulating phagocytes, contributing to prolonged circulation times and highly efficient tumor accumulation. Using free Cy7 as a low-molecular-weight model drug control, our nanocarrier platform is shown to be able to massively improve the delivery of small molecules to the pathological site. As compared to liver and spleen, tumor accumulation was a 2–3 fold higher. Interestingly, in addition to prominent targeting of CCPM to tumor, liver and spleen, we observed accumulation in lung and in bone marrow. While the cellular uptake of CCPM in these tissues needs to be analyzed in future studies, the latter finding indicates that the micelles may also be useful for targeting myeloid and lymphoid progenitor cells, opening up interesting opportunities for immunomodulatory therapy, as well as for the treatment of non-oncological disorders.

Besides commonly perceived functions attributed to the liver, such as metabolic and storage activity, protein synthesis and detoxification, increasing importance is being given to the hepatic immune system. In this regard, the liver has recently been recognized as an active immunological organ in several different situations [30–33]. Along the same line of thinking, the spleen as a secondary lymphoid organ contains a large number of lymphoid cells in the white pulp as well as many myeloid mononuclear phagocytic cells between the red pulp and the marginal zone [34]. Thus, the spleen crucially contributes to both innate and adaptive immune responses [35]. Having observed that the majority of i.v. administered CCPM accumulated - besides in tumor - in liver and spleen, we therefore systematically studied tissue distribution and cellular uptake in these organs. At the tissue level, CCPM were found to mostly reside extracellularly; only approximately one third was found inside cells in the three tissues analyzed. This led us to investigate by which cells the NPs are taken up.

When looking at the major cell population in 4T1 tumors, i.e. cancer cells, it was found that 1.5% were positive for CCPM uptake. This finding is in line with a previous study showing that the vast majority of i.v. injected nanomedicines remain extracellular in tumors, with only a small fraction of cancer cells (2%) being positive for NP [36]. Keeping this notion in mind, with regard to mechanism of action, sustained drug release from extracellular CCPM within the tumor interstitium and subsequent trafficking of the released cargo to cancer cells explains the potent anticancer activity and tumor-growth inhibition properties of our platform [13]. Conversely, more than 15% of immune cells in the tumor microenvironment were found to be positive for CCPM, and overall, 66% of intracellular CCPM were present in $CD45^+$ leukocytes. These patterns were similar in liver and spleen, in which we identified the majority of intracellular CCPM to be in leukocytes (mostly $F4/80^+$ phagocytes), and not in hepatocytes or splenocytes. This propensity of the CCPM to be internalized by $F4/80^+$ phagocytic immune cells points towards opportunities for the utilization of this nanocarrier platform for applications that go beyond delivery of chemotherapeutic drugs. In this regard, more insights into the spatio-temporal exposure of individual cells to the native drug are still to be generated.

Currently, CCPM are mainly used for the delivery of small-molecule chemotherapeutics, such as docetaxel. Over the years, the anticancer activity of drug-loaded CCPM has been extensively investigated and the PEG-b-pHPMA-lactate platform has been shown to be efficacious in multiple different solid tumor models [37,38]. Beyond their use for delivering chemotherapeutics, the insights presented here suggest that CCPM may also be useful for pharmacologically modulating the tumor immune microenvironment. For example, targeting drugs to M2-like pro-tumor macrophages in order to promote polarization to M1-like anti-tumor macrophages has recently emerged as a promising immunomodulatory strategy, particularly for improving the efficacy of immune checkpoint blockade therapy [39]. Finally, considering that alternative routes of administration showed CCPM to attain a high systemic availability [40], and that the targeting of distant tissues such as the lymph nodes typically requires subcutaneous administration [41], immunomodulation beyond the borders of the primary tumor may be benefited by the utilization of CCPM.

Taking everything together, we here used optical imaging to study the whole-body, tissue and cellular distribution of CCPM. Our finding that high tumor accumulation is accompanied by high uptake in phagocytic immune cells suggests potential usefulness of this delivery platform for immunomodulatory treatments as well as for combinational cancer nano-immunotherapy.

5. Conclusion

Multimodal and multiscale optical imaging was employed to investigate the biodistribution of PEG-b-pHPMA-lactate-based CCPM. This was done at the whole organism, tissue and cellular level, in mice bearing 4T1 triple-negative breast cancer tumors. CCPM achieved strong tumor accumulation, with 33% of the micelles localizing intracellularly and 67% extracellularly. The prominent extracellular localization points towards the importance of controlled and sustained drug release in the tumor microenvironment, followed by drug trafficking to cancer cells. The intracellular fraction of CCPM was primarily associated with $F4/80^+$ phagocytic immune cells, which can in the future be exploited for immunomodulatory and immunotherapy purposes.

Credit author statement

I.B., Q.S. and D.M. contributed equally to this work. I.B., Q.S., D.M., M.B., M.T., C.J.F.R., T.L., and A.M.S. designed the research. I.B., Q.S., D.M., S.R., M.B., Q.H. performed the experiments. I.B., Q.S., D.M., F.G., M.B., T.L., and A.M.S. analyzed the data. I.B., Q.S. and D.M. drafted the paper. F.G., S.R., F.K., M.B., Q.H., M.T., G.S., W.E.H., Y.S., and C.J.F.R., T.L. and A.M.S. revised the paper. All authors discussed, read and approved the submitted manuscript.

Acknowledgements

The authors gratefully acknowledge financial support by the German Research Foundation (DFG: GRK2375 (Project number: 331065168), SFB1382 (Project number: 403224013), SFB/TRR57 and SFB1066), the European Research Council (ERC; Meta-Targeting; Project number: 864121), the European Union (European Fund for Regional Development: TAKTIRA; Project number: EFRE-0801767), and the Aachen Interdisciplinary Center for Clinical Research (IZKF; Project number: O3-2).

Appendix A. Supplementary data

Supplementary data to this article can be found online at https://doi.org/10.1016/j.jconrel.2020.09.046.

References

[1] D. Peer, J.M. Karp, S. Hong, O.C. Farokhzad, R. Margalit, R. Langer, Nanocarriers as an emerging platform for cancer therapy, Nat. Nanotechnol. 2 (2007) 751–760, https://doi.org/10.1038/nnano.2007.387.

[2] A.C. Anselmo, S. Mitragotri, Nanoparticles in the clinic: an update, Bioeng. Transl. Med. (2019), https://doi.org/10.1002/btm2.10143.

[3] H. Cabral, K. Miyata, K. Osada, K. Kataoka, Block copolymer micelles in nanomedicine applications, Chem. Rev. 118 (2018) 6844–6892, https://doi.org/10.1021/acs.chemrev.8b00199.

[4] J. Kopeček, Polymer–drug conjugates: origins, progress to date and future directions, Adv. Drug Deliv. Rev. 65 (2013) 49–59, https://doi.org/10.1016/J.ADDR.2012.10.014.

[5] H. Maeda, Tumor-selective delivery of macromolecular drugs via the EPR effect: background and future prospects, Bioconjug. Chem. 21 (2010) 797–802.

[6] V. Torchilin, Tumor delivery of macromolecular drugs based on the EPR effect, Adv. Drug Deliv. Rev. 63 (2011) 131–135, https://doi.org/10.1016/j.addr.2010.03.011.

[7] E. Blanco, H. Shen, M. Ferrari, Principles of nanoparticle design for overcoming biological barriers to drug delivery, Nat. Biotechnol. 33 (2016) 941–951.

[8] M. Talelli, M. Barz, C.J. Rijcken, F. Kiessling, E. Wim, Core-crosslinked polymeric micelles: principles, preparation, biomedical applications and clinical translation, Nano Today 10 (2015) 93–117.

[9] C.J. Rijcken, C.J. Snel, R.M. Schiffelers, C.F. Van Nostrum, W.E. Hennink, Hydrolysable core-crosslinked thermosensitive polymeric micelles: synthesis, characterisation and in vivo studies, Biomaterials 28 (2007) 5581–5593, https://doi.org/10.1016/j.biomaterials.2007.08.047.

[10] M. Talelli, C.J.F. Rijcken, C.F. Van Nostrum, G. Storm, W.E. Hennink, Micelles based on HPMA copolymers, Adv. Drug Deliv. Rev. 62 (2010) 231–239, https://doi.org/10.1016/j.addr.2009.11.029.

[11] I. Alberg, S. Kramer, M. Schinnerer, Q. Hu, C. Seidl, C. Leps, N. Drude, D. Möckel, C. Rijcken, T. Lammers, M. Diken, M. Maskos, S. Morsbach, K. Landfester, S. Tenzer, M. Barz, R. Zentel, Polymeric nanoparticles with neglectable protein corona, Nano Micro. Small 1907574 (2020), https://doi.org/10.1002/smll.201907574.

[12] Q. Hu, C.J.F. Rijcken, E. Van Gaal, P. Brundel, T. Etrych, B. Weber, M. Barz, F. Kiessling, J. Prakash, G. Storm, W.E. Hennink, T. Lammers, H. Kostkova, T. Etrych, B. Weber, M. Barz, J. Prakash, G. Storm, W.E. Hennink, T. Lammers, Tailoring the physicochemical properties of core-crosslinked polymeric micelles for pharmaceutical applications, J. Control. Release (2016), https://doi.org/10.1016/j.jconrel.2016.07.012.

[13] Q. Hu, C.J. Rijcken, R. Bansal, W.E. Hennink, G. Storm, J. Prakash, Complete regression of breast tumour with a single dose of docetaxel-entrapped core-crosslinked polymeric micelles, Biomaterials 53 (2015) 370–378, https://doi.org/10.1016/j.biomaterials.2015.02.085.

[14] F. Atrafi, H. Dumez, R.H.J. Mathijssen, C.W. Menke-van der Houven van Oordt, C.J.F. Rijcken, R. Hanssen, F.A.L.M. Eskens, P. Schöffski, A phase I dose-escalation and pharmacokinetic study of a micellar nanoparticle with entrapped docetaxel (CPC634) in patients with advanced solid tumours, J. Control. Release 325 (2020) 191–197, https://doi.org/10.1016/j.jconrel.2020.06.020.

[15] F. Atrafi, R.A.G. van Eerden, M.A.M. van Hylckama Vlieg, E. Oomen-de Hoop, P. de Bruijn, M.P. Lolkema, A. Moelker, C.J. Rijcken, R. Hanssen, A. Sparreboom, F.A.L.M. Eskens, R.H.J. Mathijssen, S.L.W. Koolen, Intratumoral comparison of nanoparticle entrapped docetaxel (CPC634) with conventional docetaxel in patients with solid tumors, Clin. Cancer Res. (2020), https://doi.org/10.1158/1078-0432.CCR-20-0008.

[16] R. Kedmi, N. Veiga, S. Ramishetti, M. Goldsmith, D. Rosenblum, N. Dammes, I. Hazan-halevy, L. Nahary, S. Leviatan-ben-arye, M. Harlev, M. Behlke, I. Benhar, J. Lieberman, D. Peer, A modular platform for targeted RNAi therapeutics, Nat. Nanotechnol. 13 (2018) 214–219, https://doi.org/10.1038/s41565-017-0043-5.

[17] Q. Cheng, T. Wei, L. Farbiak, L.T. Johnson, S.A. Dilliard, D.J. Siegwart, Selective organ targeting (SORT) nanoparticles for tissue-specific mRNA delivery and CRISPR–Cas gene editing, Nat. Nanotechnol. 15 (2020) 313–320, https://doi.org/10.1038/s41565-020-0669-6.

[18] J. Tang, S. Baxter, A. Menon, A. Alaarg, B.L. Sanchez-gaytan, F. Fay, Y. Zhao, C. Pérez-medina, Z.A. Fayad, T. Reiner, W.J.M. Mulder, Immune cell screening of a nanoparticle library improves atherosclerosis therapy, PNAS 113 (2016) E6731–E6740, https://doi.org/10.1073/pnas.1609629113.

[19] B.J. Crielaard, C.J.F. Rijcken, L. Quan, S. van Deer Wal, I. Altintas, M. van der Pot, J.A.W. Kruijtzer, R.M.J. Liskamp, R.M. Schiffelers, C.F. van Nostrum, W.E. Hennink, D. Wang, T. Lammers, G. Storm, Glucocorticoid-loaded core-crosslinked polymeric micelles with tailorable release kinetics for targeted rheumatoid arthritis therapy, Angew, Chemie Int. Ed. 51 (2012) 7254–7258, https://doi.org/10.1002/anie.201202713.Glucocorticoid-loaded.

[20] F. Gremse, B. Theek, S. Kunjachan, W. Lederle, A. Pardo, S. Barth, T. Lammers, U. Naumann, F. Kiessling, Absorption reconstruction improves biodistribution assessment of fluorescent nanoprobes using hybrid fluorescence-mediated tomography, Theranostics 4 (2014) 960–971, https://doi.org/10.7150/thno.9293.

[21] F. Gremse, M. Stärk, J. Ehling, J.R. Menzel, T. Lammers, F. Kiessling, Imalytics preclinical: interactive analysis of biomedical volume data, Theranostics 6 (2016) 328–341.

[22] S. Rosenhain, Z.A. Magnuska, G.G. Yamoah, A. Rawashdeh, F. Kiessling, F. Gremse, Data descriptor: a preclinical micro-computed tomography database including 3 D whole body organ segmentations, Nat. Publ. Gr. (2018) 1–9, https://doi.org/10.1038/sdata.2018.294.

[23] W. Al Rawashdeh, S. Zuo, A. Melle, L. Appold, S. Koletnik, Y. Tsvetkova, N. Beztsinna, A. Pich, T. Lammers, F. Kiessling, F. Gremse, Noninvasive assessment of elimination and retention using CT-FMT and kinetic whole-body modeling, Theranostics 7 (2017) 1499–1510, https://doi.org/10.7150/thno.17263.

[24] M.A. Miller, Y. Zheng, S. Gadde, C. Pfirschke, H. Zope, C. Engblom, R.H. Kohler, Y. Iwamoto, K.S. Yang, B. Askevold, N. Kolishetti, M. Pittet, S.J. Lippard, O.C. Farokhzad, R. Weissleder, Tumour-associated macrophages act as a slow-release reservoir of nano-therapeutic Pt(IV) pro-drug, Nat. Commun. 6 (2015) 1–13, https://doi.org/10.1038/ncomms9692.

[25] A.M. Sofias, Y.C. Toner, A.E. Meerwaldt, M.M.T. van Leent, G. Soultanidis, M. Elschot, H. Gonai, K. Grendstad, Å. Flobak, U. Neckmann, C. Wolowczyk, E.L. Fisher, T. Reiner, C.L. de Davies, G. Bjørkøy, A.J.P. Teunissen, J. Ochando, C. Pérez-Medina, W.J.M. Mulder, S. Hak, Tumor targeting by αvβ3-integrin-specific lipid nanoparticles occurs via phagocyte hitchhiking, ACS Nano (2020), https://doi.org/10.1021/acsnano.9b08693 (acsnano.9b08693).

[26] E. Sadauskas, H. Wallin, M. Stoltenberg, U. Vogel, P. Doering, A. Larsen, G. Danscher, Kupffer cells are central in the removal of nanoparticles from the organism, Part Fibre Toxicol. 4 (2007), https://doi.org/10.1186/1743-8977-4-10.

[27] S. Sindhwani, A.M. Syed, J. Ngai, B.R. Kingston, L. Maiorino, J. Rothschild, P. Macmillan, Y. Zhang, N.U. Rajesh, T. Hoang, J.L.Y. Wu, S. Wilhelm, A. Zilman, S. Gadde, A. Sulaiman, B. Ouyang, Z. Lin, L. Wang, M. Egeblad, W.C.W. Chan, The entry of nanoparticles into solid tumours, Nat. Mater. 19 (2020), https://doi.org/10.1038/s41563-019-0566-2.

[28] M.P. Monopoli, C. Åberg, A. Salvati, K.A. Dawson, Biomolecular coronas provide the biological identity of nanosized materials, Nat. Nanotechnol. 7 (2012) 779–786, https://doi.org/10.1038/nnano.2012.207.

[29] S. Ritz, S. Scho, N. Kotman, G. Baier, A. Musyanovych, J. Kuharev, K. Landfester, H. Schild, O. Jahn, S. Tenzer, V. Mailänder, Protein Corona of nanoparticles: distinct proteins regulate the cellular uptake, Biomacromolecules 16 (2015) 1311–1321, https://doi.org/10.1021/acs.biomac.5b00108.

[30] P. Knolle, J. Schlaak, A. Uhrig, P. Kempf, K.-H. Meyer Zum Bueschenfelde, G. Gerken, Human Kupffer cells secrete IL-10 in response to lipopolysaccharide (LPS) challenge, J. Hepatol. (1995) 226–229.

[31] M.P. Callery, J. Mangino, M.W. Flye, Kupffer Cell Prostaglandin-E, Production is Amplified during Hepatic Regeneration, Hepatology, (1991), pp. 368–372.

[32] F. Heymann, J. Peusquens, I. Ludwig-portugall, M. Kohlhepp, C. Ergen, C. Martin, N. Van Rooijen, J.C. Ochando, G.J. Randolph, F. Ginhoux, C. Kurts, C. Trautwein, F. Tacke, Liver inflammation abrogates immunological tolerance induced by Kupffer cells, Hepatology (2015) 279–291.

[33] M.W. Robinson, C. Harmon, C. O'Farrelly, Liver immunology and its role in in flammation and homeostasis, Cell. Mol. Immunol. (2016) 267–276, https://doi.org/10.1038/cmi.2016.3.

[34] R.E. Mebius, G. Kraal, Structure and function of the spleen, Nat. Rev. Immunol. 5 (2005) 606–616, https://doi.org/10.1038/nri1669.

[35] V. Bronte, M.J. Pittet, The spleen in local and systemic regulation of immunity, Immunity 39 (2014) 806–818, https://doi.org/10.1016/j.immuni.2013.10.010.The.

[36] Q. Dai, S. Wilhelm, D. Ding, A.M. Syed, S. Sindhwani, Y. Zhang, Y.Y. Chen, P. MacMillan, W.C.W. Chan, Quantifying the ligand-coated nanoparticle delivery to cancer cells in solid tumors, ACS Nano 12 (2018) 8423–8435, https://doi.org/10.1021/acsnano.8b03900.

[37] J.I. Hare, T. Lammers, M.B. Ashford, S. Puri, G. Storm, S.T. Barry, Challenges and strategies in anti-cancer nanomedicine development: an industry perspective, Adv. Drug Deliv. Rev. 108 (2017) 25–38, https://doi.org/10.1016/j.addr.2016.04.025.

[38] I. Ekladious, Y.L. Colson, M.W. Grinstaff, Polymer – drug conjugate therapeutics: advances, insights and prospects, Nat. Rev. Drug Discov. 18 (2019) 273–294, https://doi.org/10.1038/s41573-018-0005-0.

[39] C.B. Rodell, S.P. Arlauckas, M.F. Cuccarese, C.S. Garris, R. Li, M.S. Ahmed, R.H. Kohler, M.J. Pittet, R. Weissleder, TLR7/8-agonist-loaded nanoparticles promote the polarization of tumour-associated macrophages to enhance cancer immunotherapy, Nat. Biomed. Eng. 2 (2018) 578–588, https://doi.org/10.1038/s41551-018-0236-8.

[40] Q. Hu, J. Prakash, C.J.F. Rijcken, W.E. Hennink, G. Storm, High systemic availability of core-crosslinked polymeric micelles after subcutaneous administration, International Journal of Pharmaceutics 514 (1) (2016) 112–120, https://doi.org/10.1016/j.ijpharm.2016.09.030.

[41] A. Schudel, D.M. Francis, S.N. Thomas, Material design for lymph node drug delivery, Nature Reviews Materials 4 (2019) 415–428, https://doi.org/10.1038/s41578-019-0110-7.